

# A computational model of a barrier discharge in air at atmospheric pressure: the role of residual surface charges in microdischarge formation

Yu V Yurgelenas<sup>1</sup> and H-E Wagner<sup>2</sup>

<sup>1</sup> General Physics Institute, Russian Academy of Science, Vavilova Str. 38, Moscow 119991, Russia

<sup>2</sup> Institute of Physics, University of Greifswald, Domstr. 10a, 17489 Greifswald, Germany

E-mail: [yyurg@inbox.ru](mailto:yyurg@inbox.ru) and [wagner@physik.uni-greifswald.de](mailto:wagner@physik.uni-greifswald.de)

Received 19 June 2006, in final form 7 August 2006

Published 1 September 2006

Online at [stacks.iop.org/JPhysD/39/4031](http://stacks.iop.org/JPhysD/39/4031)

## Abstract

A two-dimensional (axially symmetric) computational model of the microdischarge formation in a barrier discharge for short (1–2 mm) gaps in air at atmospheric pressure is proposed. A non-homogeneous electric field, caused by a residual non-uniform charging of the dielectric barriers, is considered as an important reason for the filament formation by a Townsend mechanism. The ion–electron emission from the dielectric covering the cathode is treated as the principal secondary process; the secondary emission coefficient in the model is selected to be consistent with the Paschen voltage. For an applied sinusoidal voltage, this follows the microdischarge development on a microsecond scale. It is shown that even a slight inhomogeneity of the initial electric field leads to the formation of a narrow microdischarge channel.

The two-dimensional dynamics of the radiation from a microdischarge for the case of the second positive and the first negative systems of nitrogen is simulated and compared with recent experimental data. The effects of the secondary emission coefficient and of a distribution of residual surface charges are investigated. It is shown that the level of inhomogeneity of the residual surface charge distribution does not affect the radius of the microdischarge channel, but affects its two-dimensional structure.

The proposed model explains satisfactorily the experimental results for the velocity of the cathode-directed ionizing wave and the emission of the N<sub>2</sub> second positive system from a microdischarge.

## 1. Introduction

Barrier discharges (BDs) in gas gaps take place, if at least one of the two electrodes is covered by a dielectric barrier. Typically, for BDs applications in air an alternating voltage of frequencies in the range 50 Hz–100 kHz is applied. It is well known that BDs at atmospheric pressure in air and other gases consist of many separate microdischarges (MDs), which are also referred to as filaments. Experimental and theoretical studies on the breakdown in BDs have a long history [1–6] because of many industrial applications.

Recent experimental investigations of single MDs in N<sub>2</sub>/O<sub>2</sub> mixtures have been reported in [7–9]. Spatially and temporally resolved measurements of the emission spectrum of the second positive and the first negative systems of molecular nitrogen from an MD by cross-correlation spectroscopy (CCS) technique provide the possibility to evaluate axial distributions of physical plasma parameters (reduced electric field strength and electron concentration) of a MD [7]. Under selected operation conditions, it was also possible to investigate the axially and radially resolved structure of the MD radiation [9]. However, even measurements with high resolution are

severely limited by the sensitivity of the experimental devices and provide only the possibility to evaluate spatially averaged dependences of the MD parameters [7], even though a MD channel has a complicated two-dimensional (2D) structure [9]. Therefore, numerical modelling has to be considered an important tool to provide information of the local parameters of MDs, which cannot be obtained directly from experiments as well as a means to help interpret the experimental results.

Despite the considerable progress in the understanding of microdischarge formation in BDs, the knowledge of the physical mechanisms of MDs nowadays appears to be insufficient to provide an adequate complete quantitative description. The first theory of filaments in BDs [11] was based on the assumption that MDs are of the same nature as streamer discharges, i.e. the MD originates from a single electron avalanche after an avalanche-to-streamer transition. The problem is that Raethers criterion for the avalanche-to-streamer transition [10]

$$N_e = 10^8 - 10^9,$$

where  $N_e$  is the threshold electron number in the avalanche, is usually not fulfilled under the experimental conditions being considered [1].

Reathers criterion can also be rewritten in the form

$$\int (\alpha - \eta) dx \approx 20,$$

where  $\alpha$  denotes first Townsend coefficient for ionization and  $\eta$  refers to the coefficient of electron attachment.

To simulate the MD formation for a typical applied voltage, the authors [11, 12] used  $10^2 - 10^6$  initial electrons in the first avalanche. The secondary processes such as photoemission, ion–electron emission from the cathode surface and photoionization in the gas volume were included. The photoemission was considered the dominant secondary process for MD formation [12]. The computational model [12] yielded results for the velocity of the ionizing wave (IW), current and the radiation emitted from the MD that were in qualitative agreement with the experimental data. Other computational models, e.g. [13–16] were similar to [11] or [12]. So the model proposed in [12] can be considered a typical model.

However, measurements using cross-correlation spectroscopy (CCS) were able to reveal MD properties that cannot be explained by the simulations using the model in [12]. The existence of a long (up to 100 ns and even 1  $\mu$ s) pre-breakdown phase, characterized by an exponential increase in the emission intensity in the gap, cannot be understood in terms of the model in [12]. This pre-breakdown phase was first observed in [17] and investigated in more detail in [7]. Moreover, the radiation wave directed towards the anode precedes the radiation wave directed towards the cathode as shown in the ‘simulated streak-photo’ in [12], whereas such a wave was absent in the corresponding CCS pictures. The model [12] also does not explain the periodical MDs development at the positions of the previous MDs (memory effect). In terms of the initial conditions of the MD, the model [12] ignores residual surface charges on the dielectric surfaces that remain after previous MDs. Therefore, it can be considered only as a model of a first

MD or of a MD in a single-pulse mode. The analysis of the discrepancies between the modelling results and the experimental observations can be found in [7].

In the presented paper, a computational model of the BD is proposed that aims to explain the MD formation in the ordinary (continuous) mode of a BD in air at atmospheric pressure between two plane electrodes covered with a dielectric. The proposed model includes an inhomogeneous residual electric charge distribution on the dielectric surfaces as an important cause for the filamentary nature of the BD and considers the ion–electron emission from the dielectric covering the cathode as an important process during the MD formation phase. The two-dimensional (2D) dynamics of the emission of the second positive and the first negative systems of nitrogen from the MD is simulated and compared with recent experimental data.

This model was applied first in [18] to explain the experimentally observed 2D structure of MD radiation.

## 2. Fundamentals of the model

In all the simulations carried out in the framework of the model in [12], an intense initial electron avalanche (about  $10^6$  initial electrons) was considered. This leads to a fast accumulation of positive space charges near the anode, which, in turn, leads to MD formation on the 10 ns time scale. At the same time, this initial avalanche also causes the formation of the MD to occur at random positions. Such a short time scale for MD formation may also be caused by an arbitrary choice of the secondary emission coefficient (i.e. primarily the photoemission coefficient).

If the MD formation starts with only one or a few initial electrons, then the electron number in the first avalanche is very low, even near the anode. In this case, the emitted radiation is too weak to cause considerable photoemission. Therefore, an ion–electron emission from cathode or the dielectric covering the cathode must be considered the dominant mechanism that maintains the electrical discharge process. To avoid an arbitrary time scale for a pre-breakdown stage, it is possible to select an emission coefficient that is consistent with the Paschen voltage. In this case, the time scale of the process expands to the microsecond scale. The assumption of a constant applied voltage is no longer valid, and the actual time-dependence of the voltage must be taken into account.

The next step involves taking into account the residual surface charges on the dielectrics covering the cathode and anode. Their existence and their spatial distributions across the surfaces of the dielectrics have been discussed, e.g. in [4]. The expected effects of their inclusion in the model are:

- they reduce the applied voltage necessary for MD formation;
- they lead to a memory effect (new MDs originate in the same spot where the previous MD occurred).

It is necessary to separate electron emission from the dielectric cathode itself and the emission of the electrons accumulated on the surface (‘adsorbed’ electrons) [19]. It was shown in [19] that adsorbed electrons cannot play an important role in ion–electron emission because of their low surface density.

Photon-induced processes, namely photoionization in the volume and photoemission from the cathode, can also play a

role in the MD development. Photoionization in the oxygen–nitrogen mixtures utilizes photons of the wavelength range  $98 \text{ nm} < \lambda < 102.5 \text{ nm}$  [20], which are able to ionize oxygen molecules, while their absorption by nitrogen molecules is negligible.

The impact of photoionization processes on the development of filamentary discharges is not as clear as it appears from some accounts in the literature. Recent data obtained in [21] demonstrate the existence of this process, even for relatively large  $pd$  values ( $p$  is pressure and  $d$  is distance from the radiation source). Usually an account of photoionization in air-like mixtures is based on the approximations given in [20,22]. However, these data are valid only for quasi-stationary emission conditions but do not apply to the transient propagation of an ionization front. In [23], it was demonstrated that the quasi-stationary approximation is not applicable for a description of the population of  $N_2(C)$  species and  $N_2^+(B)$  species in a streamer discharge. This conclusion can also be extended to other excited species. In the case of a MD, both quasi-stationary and transient phases exist. For the phase of the propagation of the IW across the gap, the approximations [20,22] are problematic, but there are no other reliable data on photoionizing radiation in the literature.

Photoemission from the cathode can be caused by the same radiation that can cause photoionization [16]. However, photoionization produces electrons in the vicinity of the MD plasma, while the photoemission intensity at the cathode dielectric is much weaker due to a geometrical factor that varies with distance  $r$  from the ionization front as  $r^{-2}$ . Therefore, it is possible to neglect photoemission relative to photoionization during the formation stage of the MD. However, photoemission must be taken into account during the MD quenching phase during which an expansion of the MD across the cathode surface occurs. Since we focus on the MD formation here, we exclude photoemission from our model and terminate our simulation after an ionization front arrives at the cathode just before the start of the MD quenching phase.

Another question that must be addressed is the possibility of the emission of adsorbed electrons. If their bond energy is in the range 1–2 eV [19], they can be ejected by photons with energy corresponding to the (0–0) band of the  $N_2$  second positive system whose intensity is relatively high. However, there are no experimental confirmations of this process.

Finally, the initial conditions and the boundary conditions in the proposed physical model can be summarized as follows:

- (1) a sinusoidal anode voltage is applied;
- (2) residual surface charges are present on the dielectrics at the beginning and further accumulation of electric charges occurs on the dielectric surfaces;
- (3) the discharge process starts as soon as the Paschen voltage across the gap is achieved;
- (4) a low initial electron concentration is assumed initially;
- (5) secondary processes such as ion–electron emission from the cathode dielectric and photoionization in a gas volume are considered; the ion–electron emission coefficient is chosen to be consistent with the Paschen voltage.

**Table 1.** Elementary processes considered in the model.

(1) $O_2 + e \rightarrow O_2^+ + e + e$
(2) $N_2 + e \rightarrow N_2^+ + e + e$
(3) $O_2 + O_2 + e \rightarrow O_2^- + O_2$
(4) $O_2 + N_2 + e \rightarrow O_2^- + N_2$
(5) $O_2 + e \rightarrow O^- + O$
(6) $O^- + O_2 \rightarrow O_3 + e$
(7) $O^- + O_2 \rightarrow O + O_2^-$
(8) $O_2^- + O_2 \rightarrow O_2 + O_2 + e$
(9) $O_2^- + N_2 \rightarrow O_2 + N_2 + e$
(10) $N_2 + e \rightarrow N_2(A^1\Sigma_u^+) + e$
(11) $N_2(A^1\Sigma_u^+) + O_2 \rightarrow N_2 + O_2(a^1\Delta_g)$
(12) $N_2(A^1\Sigma_u^+) + O_2 \rightarrow N_2 + O + O$
(13) $N_2(A^1\Sigma_u^+) + O_2^- \rightarrow N_2 + O_2 + e$
(14) $N_2(A^1\Sigma_u^+) + O^- \rightarrow N_2 + O + e$
(15) $N_2 + e \rightarrow N_2(a^1\Sigma_u^-) + e$
(16) $N_2(a^1\Sigma_u^-) + N_2 \rightarrow N_2(B) + N_2$
(17) $N_2(a^1\Sigma_u^-) + O_2 \rightarrow N_2 + O + O$
(18) $N_2(a^1\Sigma_u^-) + O_2^- \rightarrow N_2 + O_2 + e$
(19) $N_2(a^1\Sigma_u^-) + O^- \rightarrow N_2 + O + e$
(20) $N_2(a^1\Sigma_u^-) + N_2(a^1\Sigma_u^-) \rightarrow N_4^+ + e$
(21) $N_2(a^1\Sigma_u^-) + N_2(A^1\Sigma_u^+) \rightarrow N_4^+ + e$
(22) $e + O_2 \rightarrow O_2(a^1\Delta_g) + e$
(23) $O_2(a^1\Delta_g) + O_2^- \rightarrow O_2 + O_2 + e$
(24) $O_2(a^1\Delta_g) + O^- \rightarrow O_3 + e$
(25) $O_2(a^1\Delta_g) + O_2 \rightarrow O_2 + O_2$
(26) $e + A_2^+ \rightarrow A + A, A = O, N$
(27) $e + e + A^+ \rightarrow e + A, A = O_2, N_2$
(28) $e + A^+ + B \rightarrow A + B, A, B = O_2, N_2$
(29) $A^- + B^+ \rightarrow A + B, A = O_2, O, B = O_2, N_2$

### 3. Description of the model

#### 3.1. Elementary processes and basic equations

**3.1.1. Elementary processes and reaction rates.** The air is simulated by a mixture of 20%  $O_2$  and 80%  $N_2$  (synthetic dry air) at atmospheric pressure.

The elementary processes taken into account are given in table 1. The respective reaction rate coefficients are taken from [24–26].

**3.1.2. Basic equations.** An axially symmetric drift-diffusion model of the MD is employed. The dynamic development of the BD is described by a set of continuity equations for the densities of the charged and excited particles:

$$\frac{\partial n_e}{\partial t} + \frac{\partial(n_e u_{ez})}{\partial z} + \frac{1}{r} \frac{\partial(r n_e u_{er})}{\partial r} - \frac{\partial}{\partial z} \left( D_e \frac{\partial n_e}{\partial z} \right) - \frac{1}{r} \frac{\partial}{\partial r} \left( r D_e \frac{\partial n_e}{\partial r} \right) = q_e + I_{ph}, \quad (1)$$

$$\frac{\partial n_+}{\partial t} + \frac{\partial}{\partial z} (n_+ u_{+z}) + \frac{1}{r} \frac{\partial}{\partial r} (r n_+ u_{+r}) = q_+ + I_{ph}, \quad (2)$$

$$\frac{\partial n_-}{\partial t} + \frac{\partial}{\partial z} (n_- u_{-z}) + \frac{1}{r} \frac{\partial}{\partial r} (r n_- u_{-r}) = q_-, \quad (3)$$

$$\frac{\partial n_k^*}{\partial t} = q_k^*, \quad (4)$$

and the Poisson equation is used for electrical potential

$$-\frac{\partial^2 \varphi}{\partial z^2} - \frac{1}{r} \frac{\partial}{\partial r} \left( r \frac{\partial \varphi}{\partial r} \right) = \rho / (\epsilon \epsilon_0), \quad E = -\nabla \varphi, \quad (5)$$

$$\rho = e(n_+ - n_- - n_e). \quad (6)$$

Here,  $n_e$ ,  $n_+$ ,  $n_-$ ,  $n_k^*$  denote the density of, respectively, the electrons, the positive and negative ions, and the excited

**Table 2.** Population kinetics of  $N_2(C^3\Pi_u, v=0)$  and  $N_2^+(B^2\Sigma_u^+, v=0)$  [27].

$N_2(X, v') + e \rightarrow N_2(C, v) + e$	$N_2(X, v') + e \rightarrow N_2^+(B, v) + e + e$
$N_2(C, v) + N_2(X) \rightarrow N_2(a') + N_2(X)$	$N_2^+(B, v) + N_2(X) \rightarrow N_2^+(A) + N_2(X, v')$
$N_2(C, v) + O_2(X) \rightarrow N_2(X) + O + O$	$N_2^+(B, v) + O_2(X) \rightarrow N_2^+(A) + O_2^*$
$N_2(C, v) \rightarrow N_2(B, v') + h\nu$	$N_2^+(B, v) + O_2(X) + \text{molecule} \rightarrow \text{products}$
	$N_2^+(B, v) \rightarrow N_2^+(X, v') + h\nu$

particles,  $q_\alpha(|E|, \dots, n_\alpha, \dots)$  denote the source terms due to the plasma kinetics ( $q_+ = q_e + q_-$ ),  $I_{\text{ph}}$  refers to the source term due to photoionization of the gas molecules,  $u_\alpha(|E|)$  are the drift velocities of the plasma components,  $D_e(|E|)$  is the electron diffusion coefficient and  $\rho$  denotes the space charge density.

The local dependences of all kinetic coefficients on the reduced electric field strength  $|E|/N$  are included in the model. All positive ions are considered collectively as ‘generalized positive ions’.

**3.1.3. Photoionization.** The electron sources due to photoionization are expressed by the integral [20]

$$I_{\text{ph}}(\mathbf{x}) = \frac{p_\tau}{p + p_\tau} \left( \frac{\xi\omega}{\alpha} \right)_{\text{eff}} \int \frac{v_i(\mathbf{x}') n_\epsilon(\mathbf{x}') f(r)}{4\pi r^2} d^3\mathbf{x}'. \quad (7)$$

Here,  $r = |\mathbf{x} - \mathbf{x}'|$ ,  $p_\tau$  denotes the quenching pressure,  $v_i(\mathbf{x}')$  is the ionization rate,  $\alpha(\mathbf{x}')$  is the first Townsend coefficient,  $\omega(\mathbf{x}')$  refers to the number of photons ‘produced’ by electron collisions with molecules per unit length that have sufficient energy for photoionization,  $\xi$  is the efficiency of photoionization and  $f(r)$  is an absorption function defined by

$$f(r) = \frac{\exp(-\kappa_{\min} p_{O_2} r) - \exp(-\kappa_{\max} p_{O_2} r)}{r \ln(\kappa_{\max}/\kappa_{\min})}. \quad (8)$$

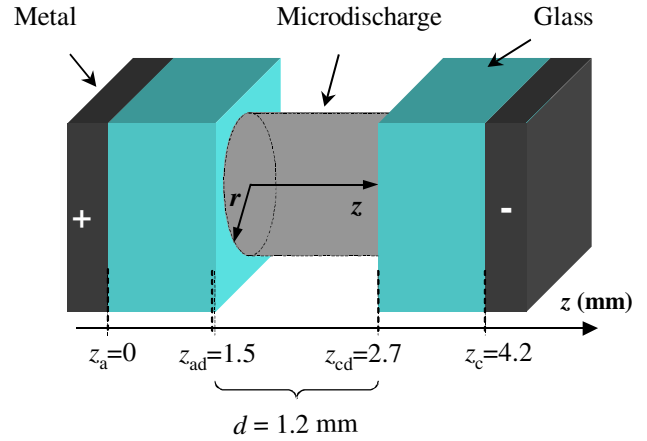
Here,  $\kappa_{\max} = 2 \text{ cm}^{-1} \text{ Torr}^{-1}$  and  $\kappa_{\min} = 3.5 \cdot 10^{-2} \text{ cm}^{-1} \text{ Torr}^{-1}$  denote the maximum and minimum absorption coefficients in a given wavelength range. From [20], one obtains  $(\xi\omega/\alpha)_{\text{eff}} \approx 0.08$ , which can be considered a constant.

The above described model corresponds to the assumption that populations of the appropriate excited radiating molecules are proportional to the local ionization rate (quasi-stationary approximation).

**3.1.4. Emission of the second positive and the first negative systems of nitrogen from a MD.** The photons production rates of the (0–0) bands of the  $N_2$  second positive system (337.1 nm) and the  $N_2^+$  first negative system (391.4 nm) are calculated according to formula

$$I_{\alpha \rightarrow \beta} = A_{\alpha \rightarrow \beta} n_\alpha,$$

where  $A_{\alpha \rightarrow \beta}$  is the transition rate for spontaneous emission  $\alpha \rightarrow \beta$  and  $n_\alpha$  is the number density of species in the excited state  $\alpha$ . The kinetic scheme for the population of  $N_2(C^3\Pi_u, v=0)$  and  $N_2^+(B^2\Sigma_u^+, v=0)$  proposed in [27] (see table 2) and the reaction rates calculated there are used in our model.


**Figure 1.** BD geometry.

(This figure is in colour only in the electronic version)

### 3.2. Initial conditions and boundary conditions

The BD geometry under consideration is shown in figure 1. Two parallel plate electrodes are covered by glass as the dielectric. The dimensions are as follows: gas gap width  $d = 1.2 \text{ mm}$  and the thickness of the dielectric material is  $1.5 \text{ mm}$ . These dimensions are similar to the experimental conditions used in [7]. The dielectric constants are assumed to be  $\epsilon = 1$  for the gas gap and  $\epsilon = \epsilon_d = 5$  for the dielectrics. Inside the dielectrics we assume  $\rho = 0$ .

The BD operates in synthetic air at atmospheric pressure and  $T = 300 \text{ K}$ .

A sinusoidal voltage  $U = U_a \sin(2\pi ft + \varphi_0)$  is applied to the electrodes. The electron emission current from the cathode is assumed to be proportional to the incoming positive ions current:

$$J_e(r, z_{cd}, t) = \gamma_1 J_e(r, z_{cd}, t). \quad (9)$$

Here, the ion–electron emission coefficient  $\gamma_1$  is estimated to be consistent with the Paschen voltage using the Townsend criterion:

$$\frac{\gamma_1 \alpha (e^{(\alpha-\eta)d} - 1)}{\alpha - \eta} = 1, \quad (10)$$

where the coefficients are calculated for the Paschen voltage applied across the gap.

For the gap width and gas pressure being considered, the Paschen voltage corresponds to the reduced electric field strength in the gap  $(E/N)_P = 169 \text{ Td}$ . Thus from (10) we obtain  $\gamma_1 = 0.006$ . In this case, the electric field strength in the gap is  $E_P = 41.33 \text{ kV cm}^{-1}$  that corresponds to the applied voltage  $U_P = 7.44 \text{ kV}$ .

The accumulation of the surface charges is described by the following equations for the surface charge densities on the

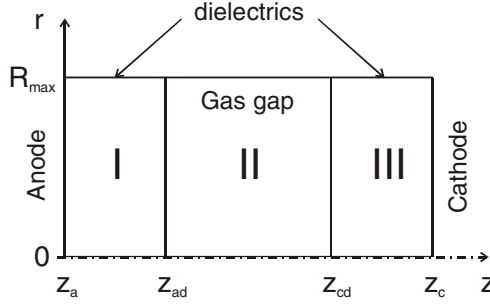


**Figure 2.** Definition of the various domains for the computation.

dielectrics near the anode  $\sigma_a(r, t)$  and near the cathode  $\sigma_c(r, t)$ :

$$\frac{\partial \sigma_a}{\partial t} = -|J_e(r, z_{ad}, t) + J_-(r, z_{ad}, t)|, \quad (11)$$

$$\frac{\partial \sigma_c}{\partial t} = |J_e(r, z_{cd}, t)| + |J_+(r, z_{cd}, t)|. \quad (12)$$

Here,  $J_e$ ,  $J_+$  and  $J_-$  denote the current densities for electrons, positive and negative ions, respectively, at the dielectric surfaces.

The initial surface charge density is taken as

$$\sigma_a|_{t=0} = -\sigma_c|_{t=0} = \sigma_0 + eN_0 \exp(-r^2/r_0^2)/(\pi r_0^2). \quad (13)$$

Here,  $\sigma_0$  is a uniform charge density and the additional term describes a disturbance that is assumed to be Gaussian with characteristic parameters  $N_0$  and  $r_0$ .

The simulations begin at the time when the electric field strength in the gap is high enough to sustain a Townsend discharge. This time is considered  $t = 0$ , with an appropriate value of the parameter  $\varphi_0$ . At this time, we assume an initial electrons density  $n_e(r, z, 0) = n_0$ .

The domain on the  $(z, r)$  plane in which the computation is carried out is shown in figure 2. It consists of: (I) the near-anode dielectric  $z_a < z < z_{ad}$ , (II) the gas gap  $z_{ad} < z < z_{cd}$  ( $z_{cd} - z_{ad} = d$  is the gap distance) and (III) the near-cathode dielectric  $z_{cd} < z < z_c$ . The maximum value of the radius used  $R_{\max} = 3$  mm is sufficiently large, so that the computational results are independent of its choice.

The continuity equations for the charged and excited particles (1)–(4) are solved in domain II. The initial concentrations of the particles are given by:

$$\begin{aligned} n_e(r, z, 0) &= n_0(r, z), \\ n_+(r, z, 0) &= n_-(r, z, 0) = n_k^*(r, z, 0) = 0. \end{aligned} \quad (14)$$

The boundary conditions for the continuity equations are:

(1) at the near-anode dielectric

$$\frac{\partial n_e}{\partial z}(r, z_{ad}, t) = 0, \quad n_+(r, z_{ad}, t) = 0, \quad (15)$$

(2) at the near-cathode dielectric

$$J_e(r, z_{cd}, t) = \gamma_i J_+(r, z_{cd}, t), \quad n_-(r, z_{cd}, t) = 0, \quad (16)$$

(3) on the axis  $r = 0$

$$\frac{\partial n_e}{\partial r}(0, z, t) = 0, \quad (17)$$

(4) At the artificial boundary  $r = R_{\max}$

$$\begin{aligned} \frac{\partial n_e}{\partial r}(R_{\max}, z, t) &= 0, \\ (n_+ u_{+r})(R_{\max}, z, t) &= (n_- u_{-r})(R_{\max}, z, t) = 0. \end{aligned} \quad (18)$$

The Poisson equation (5) is solved in the entire domain. Inside the dielectrics, it is reduced to the Laplace equation. The boundary conditions are:

(1) on the anode and cathode surfaces

$$\varphi(r, z_a, t) = U(t), \quad \varphi(r, z_c, t) = 0, \quad (19)$$

(2) on the axis  $r = 0$  and at the artificial boundary  $r = R_{\max}$

$$\frac{\partial \varphi}{\partial r}(0, z, t) = 0, \quad \frac{\partial \varphi}{\partial r}(R_{\max}, z, t) = 0, \quad (20)$$

(3) at the near-anode dielectric

$$\begin{aligned} \frac{\partial \varphi}{\partial z}(r, z_{ad}+, t) &= \varepsilon_d \frac{\partial \varphi}{\partial z}(r, z_{ad}-, t) + \frac{\sigma_a(r, t)}{\varepsilon_0}, \\ \varphi(r, z_{ad}+, t) &= \varphi(r, z_{ad}-, t), \end{aligned} \quad (21)$$

(4) at the near-cathode dielectric

$$\begin{aligned} \frac{\partial \varphi}{\partial z}(r, z_{cd}-, t) &= \varepsilon_d \frac{\partial \varphi}{\partial z}(r, z_{cd}+, t) - \frac{\sigma_c(r, t)}{\varepsilon_0}, \\ \varphi(r, z_{cd}+, t) &= \varphi(r, z_{cd}-, t). \end{aligned} \quad (22)$$

#### 4. The numerical procedure

For a finite-difference approximation of the problem described by the set of equations, initial and boundary conditions (1)–(22), we use a monotonic fully conservative high-resolution two-dimensional numerical scheme [28].

For the continuity equations (1)–(4), the scheme [28] is based on Van Leer's MUSCL approach [29], which was adapted for gas discharge problems in [30]. For ion transport, a 2D method is constructed simply by 1D splitting. For electron transport, a genuinely 2D method is used, which is based on Colella's approach [31] leading to a less restrictive Courant condition. An implicit algorithm for the account of diffusion term was proposed in [28].

For the solution of the Poisson equation (5), an iterative alternating directions implicit algorithm is used similarly to [28]. Additionally, we apply sub-domain decomposition to improve the convergence of the algorithm. Iterations in the sub-domains I, II and III were carried out in the following sequence:

- (1) Solution of Poisson equation in domain II with given values of the potential on the left and right boundaries.
- (2) Solution of the Laplace equation in domain I with given values of the potential on the left boundary and an electric field component  $E_z$  on the right boundary determined from the boundary conditions.
- (3) Solution of the Laplace equation in domain III with given values of the potential on the right boundary and an electric field component  $E_z$  on the left boundary determined from the boundary conditions.

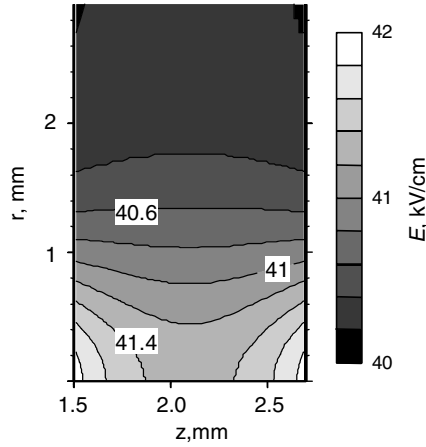


**Figure 3.** The initial electric field distribution in an air gap  $|E(r, z)|$  in  $\text{kV cm}^{-1}$ .

The boundary conditions on the other boundaries are the same as described above. The iteration cycle is repeated until convergence with a given accuracy is achieved. An additional advantage of the above algorithm is the possibility to use independent grids for the various domains.

Since different MD stages have different ranges of physical parameters and different time scales, the following procedure was used to minimize a computational time.

The Townsend pre-phase and the initial part of the space-charge-dominated phase are calculated using a relatively rough grid, which is uniform in  $z$  (steps are of the order of  $20\text{--}25\ \mu\text{m}$ ) and non-uniform in  $r$  (highest resolution of the order of  $20\ \mu\text{m}$ ). During this stage, photoionization is not included because of low emission intensity.

To simulate the MD formation phase (timescale of  $\sim 100\ \text{ns}$  or less), all the quantities are interpolated into a refined mesh. Highest resolutions are  $2\text{--}4\ \mu\text{m}$  in  $r$  and  $1\text{--}4\ \mu\text{m}$  in  $z$  depending on  $r_0$ , the lowest resolution in  $z$  was  $10\ \mu\text{m}$ . At the beginning of this stage, photoionization is included.

The grid in  $z$  is refined in the front region of the MD and is adapted during its propagation. The grid adaptation procedure preserves the net points near the ionization front and avoids interpolation for high gradients. It was found that for reliable computations a spatial resolution of better than  $1\text{--}5\ \mu\text{m}$  (depending on  $r_0$ ) in both directions was necessary. However, for the simulation in the proximity of the cathode a resolution in  $z$  of better than  $1\ \mu\text{m}$  was necessary. Therefore, when the ionization front reaches a distance of  $0.1\text{--}0.2\ \text{mm}$  from the near-cathode dielectric, the mesh in  $z$  is refined again to  $1\text{--}2/3\ \mu\text{m}$ , preserving all grid points near the front.

The time steps are limited by the following conditions.

- (1) By the Courant criterion [31]  $\Delta t < C_C \min\{\Delta z/u_z, \Delta r/u_r\}$ .
- (2) By the characteristic time for plasma-kinetic reactions  $\Delta t < C_i \min\{1/\nu_{\text{chem}}\}$ ,  $\nu_{\text{chem}} = (\partial \ln n_\alpha / \partial t)$ .
- (3) By the relaxation time  $\Delta t < C_r \min\{\varepsilon_0/\sigma_p\}$ ,  $\sigma_p$  is the specific conductivity of discharge plasma.

All coefficients must be less than 1. In the present calculations, we use  $C_C = 0.9$ ,  $C_i = 0.2$ ,  $C_r = 0.2$ .

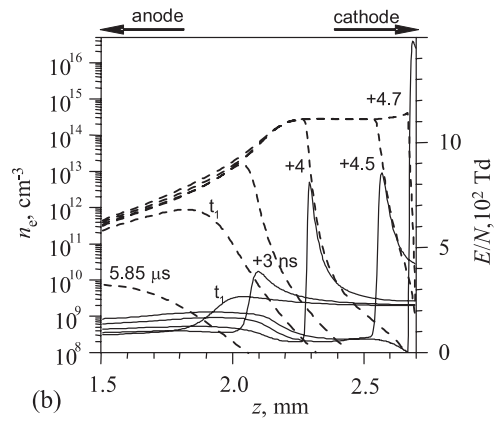
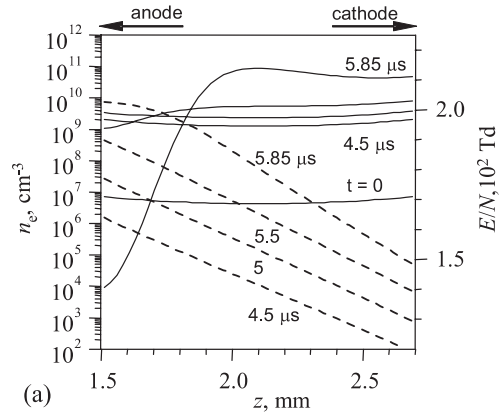


**Figure 4.** Axial distributions of the reduced electric field strength  $E/N$  (solid lines) and of the electron number density  $n_e$  (dashed lines) for different times during (a) the quasi-stationary Townsend phase and the start of the space charge phase and (b) the IW propagation (filamentary phase),  $t_1 = 5495\ \text{ns}$ .

## 5. Simulation of the microdischarge formation

The results in this section are presented for a specific set of parameters:  $U_a = 7\ \text{kV}$ ,  $f = 6.5\ \text{kHz}$ ,  $\sigma_0/e = 4.2 \cdot 10^{10}\ \text{cm}^{-2}$ ,  $n_0(r, z, t) = 10^2\ \text{cm}^{-3}$ ,  $r_0 = 0.1\ \text{cm}$  and  $N_0 = 1.4 \cdot 10^8$ . The size parameter  $r_0$  was varied from  $0.03$  to  $0.3\ \text{cm}$ ; its effect is discussed below. The calculation starts at  $U_{\text{start}} = 2.65\ \text{kV}$ .

The initial electric field distribution  $|E(r, z)|$  is shown in figure 3. The electric field strength varies along the dielectric surfaces from  $41.9\ \text{kV cm}^{-1}$  ( $r = 0$ ) to  $40.2\ \text{kV cm}^{-1}$  and along the axis from  $41.9\ \text{kV cm}^{-1}$  (left and right) to  $41.3\ \text{kV cm}^{-1}$  (middle). The maximal variation is about only 4% of the maximum electric field strength value. Because of the inhomogeneous electric field in the gap, the discharge begins near the axis before it starts in the peripheral regions. Therefore, the discharge channel is formed around the axis.

The first phase of the simulated MD can be labelled a Townsend phase of stabilization. First, the initial electrons are multiplied by ionization, but subsequently they accumulate on the anode dielectric. Subsequently, the ions dominate in the gap. Positive ions become the source of ion–electron emission from the cathode and then the electron concentration increases again. The stabilization phase lasts for several microseconds and leads to the quasi-stationary Townsend phase as shown in figure 4(a). It is characterized by an exponential temporal growth of the densities of charged particles in every position of

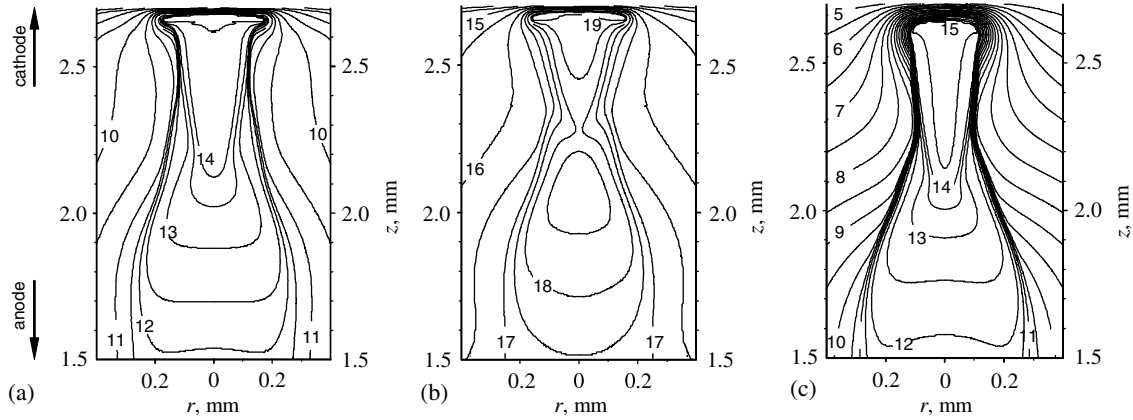


**Figure 5.** 2D distributions of the MD channel local parameters after arrival of the IW to a cathode ( $t = 5950$  ns): isolines of (a) the electron number density,  $n_e$ , in  $\text{cm}^{-3}$ , decimal logarithms (b) the emission intensity at  $\lambda = 337.1$  nm,  $I_{2+}$ , in photons  $\text{cm}^{-2} \text{s}^{-1}$ , decimal logarithms and (c) the calculated electron number density without photoionization.

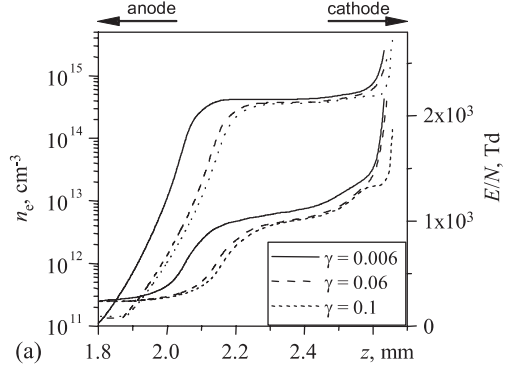
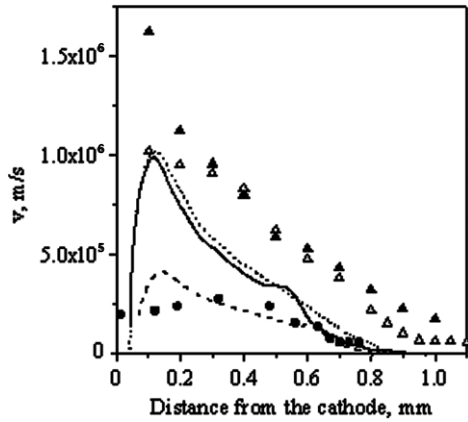


**Figure 6.** Propagation velocity of the IW in comparison with available data:  $\Delta$ : experimental values [7];  $\blacktriangle$ : experimental values [8];  $\bullet$ : calculations [4]; —: calculation for  $r_0 = 0.1$  cm; - - -: calculation for  $r_0 = 0.1$  cm (excluding photoionization);  $\cdots$ : calculation for  $r_0 = 0.04$  cm.

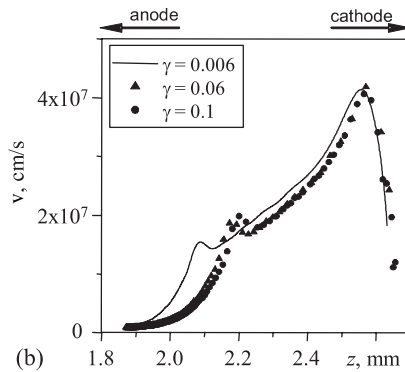
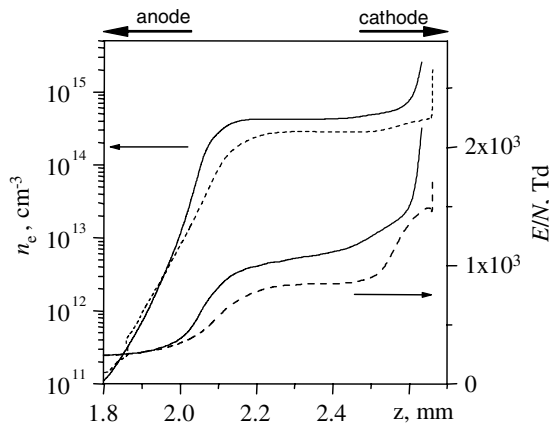
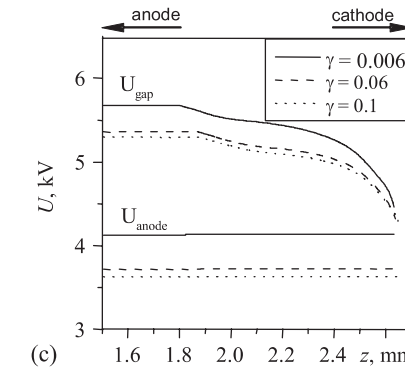


**Figure 7.** Dependence of peak values of  $n_e$  and  $E/N$  on the front coordinate during IW propagation. —: no photoionization, - - -: with photoionization.



the gap. The electron number density exponentially increases from the cathode to the anode. The subsequent space-charge-dominated phase leads to the formation of a cathode directed IW. It is characterized by a high velocity of propagation. The

**Figure 8.** Effect of the secondary emission coefficient  $\gamma_i$  on the IW propagation: Variation of (a) the peak values of  $n_e$  and  $E/N$ , (b) the velocity of the IW, (c) the anode voltage  $U_{\text{anode}}$  and the voltage drop along the axis  $U_{\text{gap}}$  with the front coordinate.

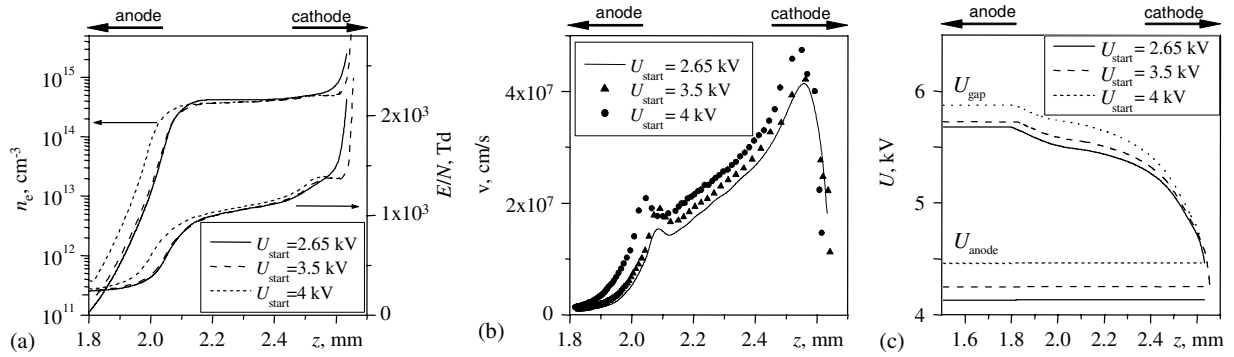


**Figure 9.** Effect of  $U_{\text{start}}$  on the IW propagation: variation of (a) the peak values of  $n_e$  and  $E/N$ , (b) the IW velocity, (c) the anode voltage  $U_{\text{anode}}$  and the gap voltage along an axis  $U_{\text{gap}}$  with the front coordinate.

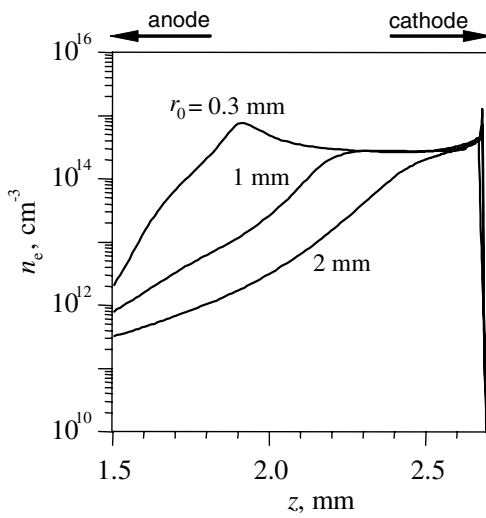


**Figure 10.** Effect of residual surface charges inhomogeneity: axial distribution of the electron number density  $n_e$  upon the IW arrival to the cathode for different values of the characteristic radius  $r_0$ .

local electric field strength is high and electron densities are large near the front of ionization. These dependences are shown in figure 4(b).

When the ionization front reaches the cathode, the following components of the MD channel can be identified in figures 4(b) and 5(a). The ‘diffuse’ part near the anode is characterized by a low electron concentration near the anode which exponentially increases towards the middle of the gap; the channel radius decreases towards the cathode. The ‘streamer’ part is characterized by a high and almost uniform electron concentration along the axis; the channel radius increases towards the cathode. The cathode layer is confined to the vicinity of the cathode dielectric. The 2D distribution of the emission intensity of the second positive system of  $N_2$  is shown in figure 5(b).

The calculated propagation velocity of the IW is shown in figure 6 together with experimental results for synthetic air [7, 8] as well as earlier calculations [4]. (The velocities obtained in [4] are calculated from the ‘simulated streak-photo’ of the MD.)

The experimental conditions in [7] are the same as in present simulation, excepting a semi-spherical shape of the electrodes (radius of dielectric surfaces  $R = 7.5$  mm). Since

MDs develop in a narrow region near the axis (about 0.3 mm radius) this difference can be considered as negligible. In [8] MDs developed in a shorter gap, for a gap width  $d = 0.9$  mm and  $R = 4.5$  mm. The results of calculations presented in [4] were obtained in the model [12] for different initial and boundary conditions, discussed in sections 1 and 2. For comparison of the results, a distance of the ionization front from the cathode dielectric is selected as a parameter.

Our calculated velocity is somewhat lower than the corresponding experimental results. A possible reason for this difference may be the omission of photoemission from the cathode in the model. Experiment and calculation agree that the velocity of the IW increases from the anode to the cathode. Near the cathode the velocity calculated here is significantly higher than that obtained in the earlier calculations [4]. Photoionization is important during the channel propagation phase and causes the high velocity of the IW (figure 6). It also causes the expansion of the BD along the cathode dielectric as shown in figure 5. If we neglect photoionization then the values of electron number density and of the reduced electric field strength at the front of ionization become higher, figure 7.

The propagation of the IW occurs at an almost constant applied voltage, similar to the model in [12]. However, this value is unknown *a priori*. The IW reaches the cathode when  $U(t) = 4.13$  kV. This value is much smaller than the voltage amplitude  $U_a = 7$  kV. In the case of  $U_{\text{start}} = 4.13$  kV under the initial conditions used here, we obtain an electron avalanche multiplication factor on the axis given by

$$\int (\alpha - \eta) dx \approx 11.8.$$

This value does not satisfy the Raether criterion. Therefore, under these conditions, a MD cannot be developed simply by an avalanche-to-streamer transition.

## 6. Effects of model parameters

### 6.1. Effect of the secondary emission coefficient

The value of  $\gamma_1$  was determined from (10) consistent with the value of the Paschen voltage, which was obtained for metallic electrodes. In reality, it can be lower or higher, if one takes into account the possible emission of the adsorbed electrons from the surface of the cathode dielectric. Here we also

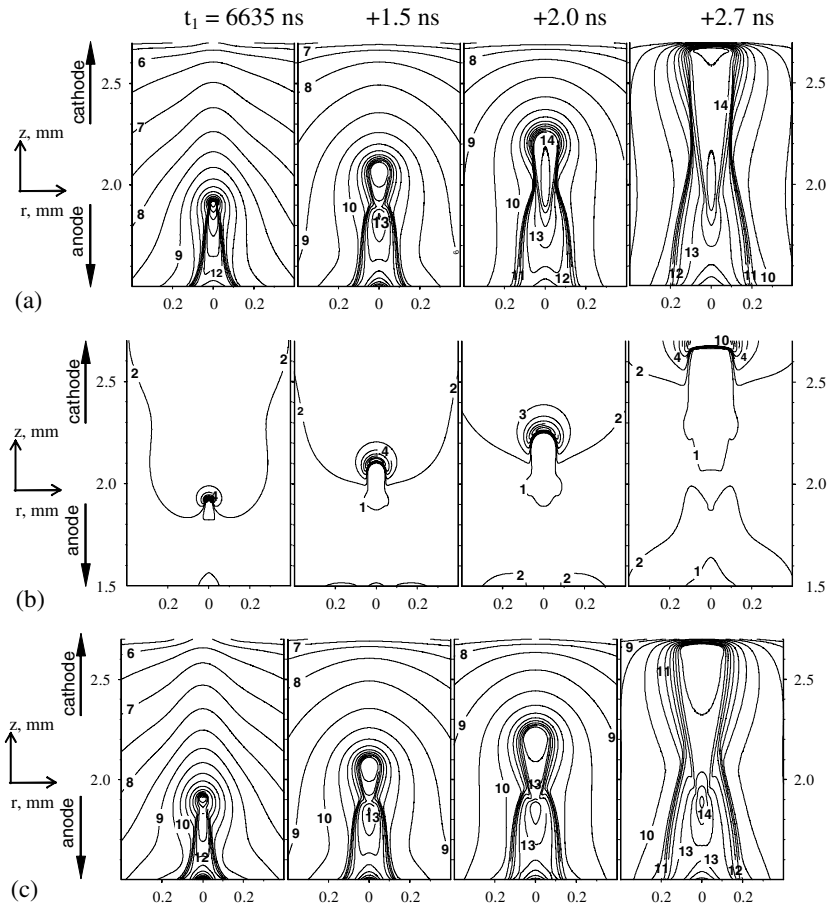


**Figure 11.** Isolines of the MD parameters during the propagation of the IW. Results of our calculations for synthetic air,  $r_0 = 0.03$  cm: (a) electron number density  $n_e$ , in  $\text{cm}^{-3}$ , decimal logarithms; (b) reduced electric field strength  $E/N$ , in 100 Td; (c) number density of  $\text{N}_2(C, v = 0)$ , in  $\text{cm}^{-3}$ , decimal logarithms.

investigated the effect of higher  $\gamma_1$  values. To avoid effects of other secondary processes, photoionization was excluded.

The simulation results are summarized in figures 8(a)–(c). The IW starts earlier (i.e. for a lower anode voltage) for larger values of  $\gamma_1$ . However, in spite of different anode voltages, the voltage drop along the axis calculated as

$$U_{\text{gap}} = \int_{z_{\text{ad}}}^{z_{\text{cd}}} E_z(0, z, t) dz,$$

at the time when the ionization front arrives to the cathode dielectric, is essentially independent of  $\gamma_1$ , figure 8(c). The difference in the velocities of the IW and in the peak values of the reduced electric field strength and electron number density on  $\gamma_1$  is not significant, figures 8(a) and (b).

The ‘boundary’ between the ‘diffuse’ and the ‘streamer’ part of the MD is closer to the cathode as the value of  $\gamma_1$  increases, so the MD is more diffuse.

## 6.2. Effect of the initial discharge voltage

For low electron number densities,  $n_e < 10^8 \text{ cm}^{-3}$ , the initial phase of the MD development is rather stochastic. Therefore, the application of the continuity equations in this case can be considered only as an ‘average over many MDs’. There is a probability that for very low initial electron concentration the

MD is quenched at a very early stage. The next ‘attempt’ to develop a MD is expected to occur for a higher initial voltage.

Therefore, we investigated the effect of  $U_{\text{start}}$  on the MD formation and its dynamics. The calculations were performed excluding a photoionization. The simulation results are presented in figures 9(a) and (c). It is clearly seen that a wide variation in  $U_{\text{start}}$  has no significant effect on the MD parameters and on the IW velocity as a function of the ionization front coordinate. For higher values of  $U_{\text{start}}$ , the boundary between the ‘diffuse’ and the ‘streamer’ part is slightly closer to the anode.

In spite of very different anode voltages, the voltage drop along the axis,  $U_{\text{gap}}$ , at the time when the ionization front arrives to the cathode dielectric, is essentially constant for different values of  $U_{\text{start}}$ , figure 9(c).

However, the time for MD channel formation shows a strong dependence on the initial voltage. It varies from  $\approx 5.96 \mu\text{s}$  for  $U_{\text{start}} = 2.65 \text{ kV}$  to  $\approx 2.05 \mu\text{s}$  for  $U_{\text{start}} = 4 \text{ kV}$ .

## 6.3. Effect of an inhomogeneous surface charge

The initial surface charge distribution (13) depends on 3 parameters: the uniform charge density  $\sigma_0$ ; the number of electrons in the non-uniform part of the surface charge  $N_0$  and the characteristic size of surface charge inhomogeneity  $r_0$ . The value of  $\sigma_0$  leads to an additional voltage across the

gap. It causes the formation of a MD at a lower anode voltage (i.e. the operating voltage is less than the ignition voltage). The most pronounced effect is expected from the localization parameter  $r_0$ , which is investigated in this section.

In the present computations, the value of  $r_0$  was varied from 0.3 to 3 mm. In every simulation we selected the appropriate value of  $U_{\text{start}}$ . However, there is no well-defined procedure to determine this value for a non-uniform electric field. As shown by the results in section 6.2, the exact choice of this value has no significant effect on the MD formation and its dynamics.

The IW velocity is essentially insensitive to the parameter  $r_0$  as shown in figure 6. However, its value affects the 2D structure of the MD channel. The ‘streamer’ part becomes considerably longer for smaller values of  $r_0$  (figure 10). On the other hand, for  $r_0 > 2$  mm, there is only a ‘diffuse’ part of the MD. This gives rise to the possibility of evaluating  $r_0$  from a comparison with experimental data [9] (see also section 7). At the same time, the maximum radius of an emitting channel depends only weakly on this parameter as the ionizing front arrives at the cathode.

For the value of  $r_0 = 0.3$  mm the calculated distance from the anode to the boundary between the ‘diffuse’ part and the ‘streamer’ part of the MD is in agreement with experimental data [9]. The temporal variations of the 2D distributions of the MD parameters in this case are presented in figures 11(a) and (c).

A pronounced filamentary structure in the MD conducting channel is clearly seen in figure 11(a). The ‘diffuse’ part and the ‘streamer’ part are clearly distinguished. The channel diameter varies from 0.4 mm near the anode to 0.2 mm in the middle to 0.3 mm near the cathode at the time of arrival at the cathode (+2.7 ns).

A region of high reduced electric field strength is localized in a confined area in front of the ionization front. Behind the ionization front, a highly conducting region develops in the ‘streamer’ part of the MD. The electric field in this region is very low. Overall, the distribution of the excited  $N_2(C, v = 0)$  molecules is very similar to the distribution of free electrons; some differences are found in the front region because of its high speed of propagation.

## 7. Modelling of the microdischarge radiation and comparison with experimental results

The radiation emitted from the MD exemplified by the emission of the (0–0) band of the  $N_2$  second positive system is investigated and compared with the experimental results.

The dependence of the emission intensity from the MD channel on  $t$  and  $z$  (spatio-temporal distribution) for the second positive system ( $\lambda = 337.1$  nm) compared with experimental data [7] is presented in figure 12. The intensity  $I(z, t)$  refers to the number of photons emitted from the channel unit length per second ( $\text{cm}^{-1} \text{s}^{-1}$ ). The emission during the pre-breakdown phase is clearly apparent. It increases with time and increases from the cathode to the anode, before it is transformed into a cathode-directed wave (also see [7]).

The calculated dynamics of the emission from the MD channel during the IW propagation in comparison with experimental data is shown in figures 13(a) and (b). Here,

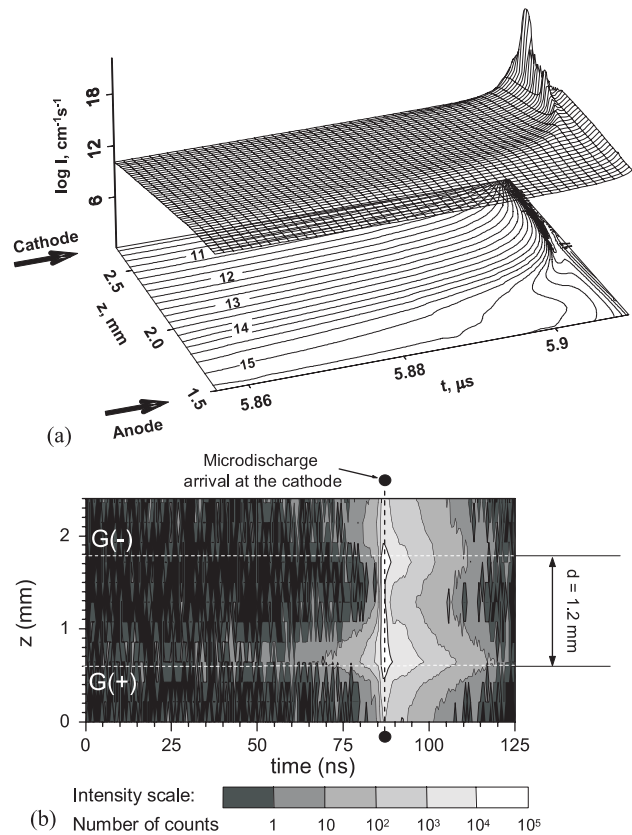


**Figure 12.** Spatio-temporal distribution of the emission intensity from the MD channel at  $\lambda = 337.1$  nm: (a) results of the numerical modelling  $I$ , photons  $\text{cm}^{-1} \text{s}^{-1}$ , (b) experimental results; G(–) and G(+) mark the polarity and level of the dielectric glass surfaces [7].

$I_{2+}(r, z)$  is the number of emitted photons per unit of area and second ( $\text{cm}^{-2} \text{s}^{-1}$ ). The intensities are integrated over the lines orthogonal to the plane of observation to allow for a direct comparison with the experimental data. In figure 13(a), experimental results are presented which correspond in the time scale to the calculated results.

The experimental results of the CCS-measurements are obtained for a mixture of 6 vol.%  $O_2$  and 94 vol.%  $N_2$ , while present simulations are made for 20 vol.%  $O_2$  and 80 vol.%  $N_2$ . However, the mechanism of the MD development does not significantly depend on the mixing ratio as was shown in [8,9].

In summary, it can be stated that the calculated 2D distributions of the emission intensity are very similar to the experimental results. In particular, the calculated channel radius 0.1–0.2 mm is the same as the experimentally determined radius. The best agreement between simulation and experiment is achieved for  $r_0 = 0.3$ –0.4 mm.

Similarly, the simulated results for the emission of the  $N_2^+$  (0–0) band of the first negative system are presented in figure 14. There are, at this time, no experimental data for a meaningful comparison.

## 8. Conclusions

We propose a Townsend model of a MD in the continuous mode of a BD in short air gaps at atmospheric pressure. The inclusion

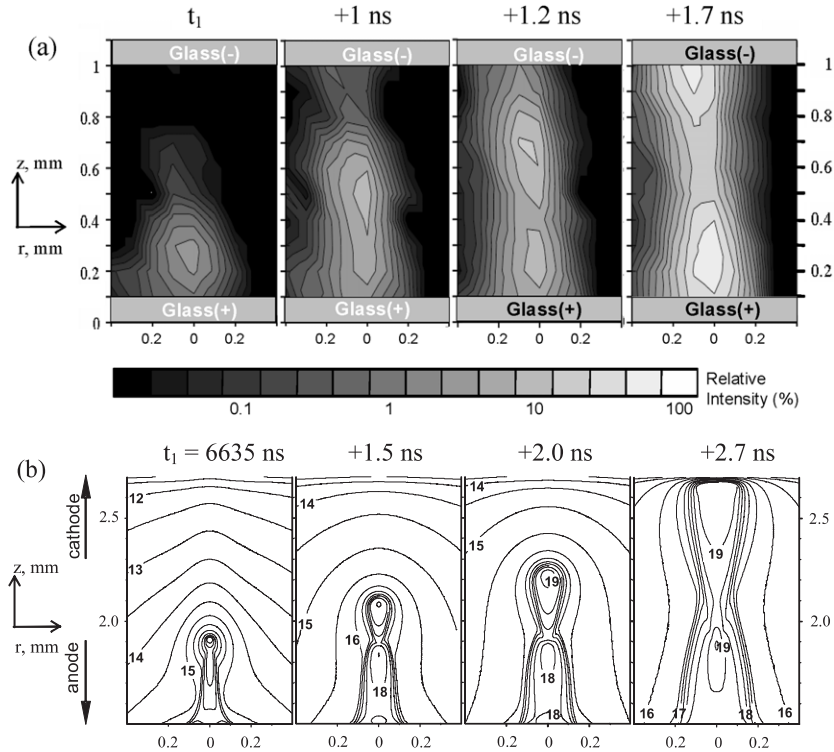


**Figure 13.** Emission intensity during the MD propagation at  $\lambda = 337.1$  nm. (a) CCS-measurements for a mixture of 6 vol.%  $O_2$  and 94 vol.%  $N_2$ . (b) Results of the calculations of  $I_{2+}(r, z)$  in photons  $cm^{-2} s^{-1}$  (decimal logarithms) for synthetic air,  $r_0 = 0.03$  cm.

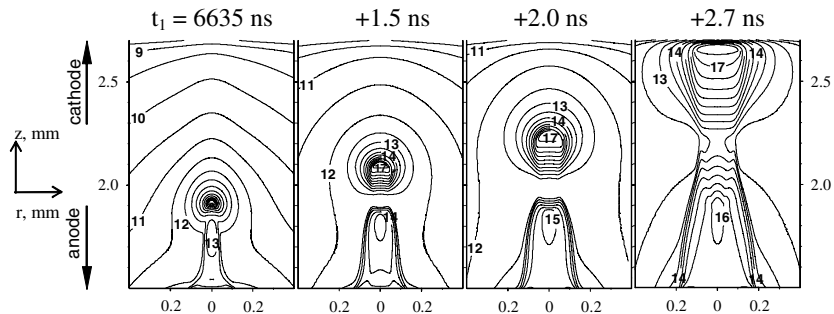


**Figure 14.** Emission intensity during the MD propagation at  $\lambda = 391.4$  nm. Results of the calculations in photons  $cm^{-2} s^{-1}$  (decimal logarithms) for synthetic air,  $r_0 = 0.03$  cm.

of ion–electron emission from the cathode dielectric as the only secondary process is sufficient to explain the formation of MDs by a Townsend mechanism. The conditions for filament formation in the proposed model are not consistent with the assumption of filament formation via a streamer mechanism, which requires higher electric field strength in the gap. Using a sinusoidal applied voltage, the MD formation takes several microseconds including the Townsend pre-phases, the space charge dominated phase and the IW propagation phase across the gap. Photoionization is not a necessary process for filament development, but it is important during the IW propagation phase, where it is responsible for the measured high velocity of the IW. An additional effect of photoionization is the expansion of the MD channel along the surface of the cathode dielectric. The comparatively long time scale for the MD formation observed here is not in contradiction with the experimental data, because a ‘visible’ phase lasts for hundreds of nanoseconds in agreement with [7, 17]. This provides a

possible explanation for the pre-breakdown emission of the  $N_2$  second positive system detected in [7, 17] for almost  $1 \mu s$  prior to the ionization wave.

It is shown here that residual surface charges on the dielectrics that remain after a MD are responsible for subsequent filament formation in the same place. The inhomogeneous electric field in a gap leads to MD formation.

The simulations show that even very small variation in the initial electric field strength in the radial direction (less than 1% of its maximal value) leads to the formation of a narrow MD channel of a radius of 0.1–0.2 mm. At the same time, the radius of a MD channel depends on this variation very weakly.

Our simulations show that a MD channel consists of a ‘diffuse’ part and a ‘streamer’ part. This corresponds to the experimental observation of emission from a MD. A MD is more ‘diffuse’ for larger values of the emission coefficient and of the characteristic radius  $r_0$  of residual surface charge non-homogeneity. A reasonable agreement between simulated

and measured 2D structures of MD emissions is achieved for  $r_0 = 0.3\text{--}0.4$  mm.

The proposed model explains the experimental results relating to the MD channel dynamics and the emitted radiation presented in [7, 9].

The main conclusions can be summarized as follows.

- (1) The proposed model explains a MD formation in the continuous mode of a BD in a short air gap at atmospheric pressure via a Townsend mechanism. Qualitatively, the simulation results are not sensitive to the following model parameters: residual surface charge distribution, secondary emission coefficient and initial voltage.
- (2) The filament formation can be caused by an inhomogeneous electric field due to residual non-uniform charging of the dielectrics after a MD. The reason is that a Townsend discharge starts earlier in the regions of higher electric field. This leads to the development of a MD in place of the previous MD (memory effect). Any singularity in the initial conditions or the boundary conditions (such as a spot of electrons or a sharp electrode) is not necessary for the development of a filamentary discharge. This mechanism also explains that the BD ignition voltage is larger than the operating voltage for continuous BDs.
- (3) The relatively long (about  $1\ \mu\text{s}$ ) pre-breakdown phase, characterized by continuously increasing emission intensity in the gap, which was detected in experiments [7, 17], corresponds to the Townsend pre-phase of a MD.
- (4) The MD channel consists of a 'diffuse' part and a 'streamer' part, which correspond to different features in the emission intensity from a MD channel as observed in experiments. The 'streamer' part is characterized by higher, axially almost uniform, electron number density, while the electron concentration exponentially decreases towards the anode in the 'diffuse' part. Depending on the initial conditions and the boundary conditions, a MD can be more 'diffuse' or more 'streamer-like'.
- (5) Photoionization can be a reason for the experimentally observed high velocity of the IW, but it is not a necessary process for MD formation.
- (6) The photon-induced processes (photoemission and photoionization) are necessary for the expansion of a MD channel across the surface of the cathode dielectric during the MD quenching phase.

## Acknowledgments

This work was supported by the Deutsche Forschungsgemeinschaft (DFG), Sonderforschungsbereich 198: 'Kinetics of partially ionized plasmas'. The authors are grateful to Dr K V Kozlov for helpful discussions and for invaluable suggestions and comments to the manuscript. The authors also express their deep gratitude to Professor K H Becker for a lot of invaluable comments to the text of the manuscript and for substantial improvement of the English text of the paper.

## References

- [1] 2005 *Non-Equilibrium Air Plasmas at Atmospheric Pressure (Series in Plasma Physics)* ed K H Becker *et al* (Bristol: Institute of Physics Publishing)

- [2] Kogelschatz U 2003 Dielectric-barrier discharges: their history, discharge physics, and industrial applications *Plasma Chem. Process.* **23** 1–45
- [3] Samoilovich V G, Gibalov V I and Kozlov K V 1997 *Physical Chemistry of the Barrier Discharge* (Düsseldorf: DVS)
- [4] Gibalov V I and Pietsch G 2000 The development of dielectric barrier discharges in gas gaps and on surfaces *J. Phys. D: Appl. Phys.* **33** 2618–36
- [5] Wagner H-E, Brandenburg R and Kozlov K V 2004 Progress in the visualization of filamentary gas discharges, Part 1: milestones and diagnostics of dielectric-barrier discharges by cross-correlation spectroscopy *J. Adv. Oxid. Technol.* **7** 11–19
- [6] Wagner H-E, Brandenburg R, Kozlov K V, Sonnenfeld A, Michel P and Behnke J F 2003 The barrier discharge: basic properties and applications to surface treatment *Vacuum* **71** 417–36
- [7] Kozlov K V, Wagner H-E, Brandenburg R and Michel P 2001 Spatio-temporally resolved spectroscopic diagnostics of the barrier discharge in air at atmospheric pressure *J. Phys. D: Appl. Phys.* **34** 3164–74
- [8] Kozlov K V, Brandenburg R, Wagner H-E, Morozov A M and Michel P 2005 Investigation of the filamentary and diffuse mode of barrier discharges in  $\text{N}_2/\text{O}_2$  mixtures at atmospheric pressure by cross-correlation spectroscopy *J. Phys. D: Appl. Phys.* **38** 518–29
- [9] Brandenburg R, Wagner H-E, Morozov A M and Kozlov K V 2005 Axial and radial development of the microdischarges of barrier discharge in  $\text{N}_2/\text{O}_2$  mixtures at atmospheric pressure *J. Phys. D: Appl. Phys.* **38** 1649–57
- [10] Reather H 1964 *Electron Avalanches and Breakdown in Gases* (London: Butterworths)
- [11] Gibalov V I, Samoilovich V G and Filippov Yu V 1981 Physical chemistry of the electrosynthesis of ozone. The results of numerical experiments *Russ. J. Phys. Chem.* **55** 471–9
- [12] Braun D, Gibalov V and Pietsch G 1992 Two-dimensional modeling of the dielectric barrier discharge in air *Plasma Sources Sci. Technol.* **1** 166–74
- [13] Yoshida K and Tagashira H 1986 Computer simulation of ozone electrosynthesis in an  $\text{N}_2/\text{O}_2$  mixture-fed ozonizer *Mem. Kitami Inst. Technol.* **18** 11–20
- [14] Eliasson B, Hirth M and Kogelschatz U 1987 *J. Phys. D: Appl. Phys.* **20** 1421–7
- [15] Li J and Dhali S K 1997 Simulation of microdischarges in a dielectric-barrier discharge *J. Appl. Phys.* **82** 4205–10
- [16] Steinle G, Neundorf D, Hiller W and Pietralla M 1999 Two-dimensional simulation of filaments in barrier discharges *J. Phys. D: Appl. Phys.* **32** 1350–6
- [17] Kozlov K, Shepeliuk O, Samoilovich V 1995 Spatio-temporal evolution of the dielectric barrier discharge channels in air at atmospheric pressure *Proc. 11th Int. Conf. on Gas Discharges and their Applications (Tokyo, Japan)* vol 2, pp 142–5
- [18] Wagner H-E, Yurgelenas Yu V and Brandenburg R 2005 The development of microdischarges of barrier discharges in  $\text{N}_2/\text{O}_2$  mixtures—experimental investigations and modelling *Plasma Phys. Control. Fusion.* **47** B641–54
- [19] Golubovskii Yu B, Maiorov V A, Behnke J and Behnke J F 2002 Influence of interaction between charged particles and dielectric surface over a homogeneous barrier discharge in nitrogen *J. Phys. D: Appl. Phys.* **35** 751–61
- [20] Zheleznyak M B, Mnatsakanyan A Kh and Szykh S V 1982 Photoionization of nitrogen-oxygen mixtures by emission from a gas discharge *Teplofiz. Vys. Temp.* **20** 423–8 (in Russian)
- [21] Aints M, Haljaste A and Roots L 2002 Photoionizing radiation of positive corona in moist air *Proc. 8th Int. Symp. on High Pressure Low Temperature Plasma Chemistry (Tartu, 21–25 July 2002)*

- [22] Penney G W and Hummert G T 1970 Photoionization measurements in air, oxygen and nitrogen *J. Appl. Phys.* **41** 572–7
- [23] Djakov A F, Bobrov Yu K and Yourguelenas Yu V 1999 Numerical modelling of air streamer discharge radiation in the second positive and first negative systems of molecular nitrogen *J. Tech. Phys.* **40** part 1, 247–50
- [24] Kossyi I A, Kostinsky A Yu, Matveyev A A and Silakov V P 1992 Kinetic scheme of the non-equilibrium discharge in nitrogen—oxygen mixtures *Plasma Sources Sci. Technol.* **1** 207–20
- [25] Eliasson B and Kogelschatz U 1986 *Basic Data for Modelling of Electrical Discharges in Gases: Oxygen Mixtures* Asea Brown Boveri Corporate Research KL 86-11 C
- [26] Diyakov A F, Bobrov Yu K, Sorokin A V and Yurgelenas Yu V 1999 *Principal Physics of Electrical Breakdown in Gases* ed A F Diyakov (Moscow: MPEI Publishers) (in Russian)
- [27] Matveev A A. and Silakov V P 1998 Method of specific radiant emittance calculation for the bands of 1– and 2+ systems of nitrogen in the non-equilibrium nitrogen-oxygen plasma *Physics and Technology of Electric Power Transmission* vol 1 ed A F Diyakov (Moscow: MPEI Publishers) pp 201–18 (in Russian)
- [28] Yourguelenas Yu V 2000 Monotonic fully conservative numerical scheme for streamer discharge simulation *Proc. 7th Int. Symp. on High Pressure Low Temperature Plasma Chemistry (Greifswald, Germany)* vol 1, eds H–E Wagner *et al* pp 159–63
- [29] Van Leer B 1977 Towards the ultimate conservative difference scheme IV. A new approach to numerical convection *J. Comput. Phys.* **23** 276–99
- [30] Bobrov Yu K and Yurgelenas Yu V 1998 Application of high-resolution schemes in the modelling of ionization waves in gas discharges *Comput. Math. Math. Phys.* **38** 1652–61
- [31] Colella P 1990 Multidimensional upwind methods for hyperbolic conservation laws *J. Comput. Phys.* **87** 171–200